J Biol Inorg Chem (2008) 13:1219–1230
DOI 10.1007/s00775-008-0405-4

ORIGINAL PAPER

Spin-state-dependent oxygen sensitivity of iron dithiolates: sulfur oxygenation or disulfide formation

Martin G. O'Toole · Majda Kreso · Pawel M. Kozlowski · Mark S. Mashuta · Craig A. Grapperhaus

Received: 18 February 2008 / Accepted: 25 June 2008 / Published online: 17 July 2008

Abstract The oxygen sensitivity of two related iron(III) dithiolate complexes of the ligand [4,7-bis-(2′-methyl-2′-mercatopropyl)-1-thia-4,7-diazacyclononane], (bmmp-TASN)FeCN (**1**) and (bmmp-TASN)FeCl (**2**), has been examined. Oxygen exposure of the low-spin complex **1** yields the disulfonate complex (bmmp-O_6-TASN)FeCN (**3**) as an olive-green solid with characteristic peaks in the IR spectrum at 1262, 1221, 1111, 1021, 947, 800, and 477 cm^{-1}. The corresponding nickel dithiolate, (bmmp-TASN)Ni (**4**), yields the related disulfonato derivative, (bmmp-O_6-TASN)Ni (**5**) upon addition of H_2O_2 (IR bands at 1258, 1143, 1106, 1012, 800, and 694 cm^{-1}. Oxygen exposure of the high-spin complex **2** results in disulfide formation and decomplexation of the metal with subsequent iron-oxo cluster formation. Complexes **1** and **2** were examined using density functional theory calculations. A natural bond order/natural localized molecular orbital covalency analysis reveals that the low-spin complex **1** contains Fe–$S_{thiolate}$ bonds with calculated covalencies of 75 and 86%, while the high-spin complex **2** contains Fe–$S_{thiolate}$ bonds with calculated covalencies of 11 and 40%. The results indicate the degree of covalency of the Fe–S bonds plays a major role in determining the reaction pathway associated with oxygen exposure of iron thiolates. The X-ray structures of **1**, **4**, and **5** are reported.

Keywords Iron thiolate · Oxygenation · Nitrile hydratase · Oxygen sensitivity · Modeling studies

Introduction

Iron-coordinated thiolates play key roles in a variety of biological systems including, but not limited to, oxygen transport and activation (heme proteins) [1, 2], electron transfer (iron–sulfur proteins) [3, 4], hydrolysis (nitrile hydratase, NHase) [5–7], antioxidant activity (superoxide dismutase and glutathione) [8, 9], and nitric oxide transport [10]. As such, several studies have been conducted to elucidate the nature of the iron–thiolate bond in a variety of coordination environments [11–23]. Nonetheless, several fundamental issues regarding their reactivity remain unresolved, including the predictability of oxygen sensitivity. While it is known that some iron thiolates are involved in oxygen transport/activation at the metal center [2, 24–26], many others react detrimentally with dioxygen, leading to disulfide formation and loss of activity [6, 7].

A notable exception is the enzyme NHase [27, 28], which requires oxygen addition to sulfur in a beneficial posttranslational modification of active-site cysteine residues to sulfur oxygenates. This non-heme iron-containing enzyme catalyzes the conversion of nitriles to amides [5–7, 29]. Among numerous unusual structural and functional features at the NHase active site are the three cysteine-derived sulfur donors, each with a different oxidation state (Fig. 1) [30]. It has since been shown that this posttranslational modification is imparted by dioxygen and is necessary for enzymatic activity [31–33]. The active site of

Electronic supplementary material The online version of this article (doi:10.1007/s00775-008-0405-4) contains supplementary material, which is available to authorized users.

M. G. O'Toole · M. Kreso · P. M. Kozlowski · M. S. Mashuta · C. A. Grapperhaus (✉)
Department of Chemistry,
University of Louisville,
Louisville, KY 40292, USA
e-mail: grapperhaus@louisville.edu

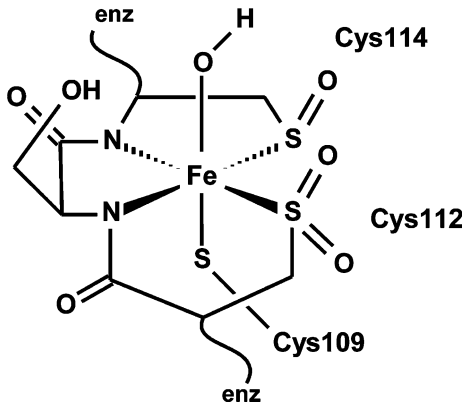

Fig. 1 Active site of iron-containing nitrile hydratase

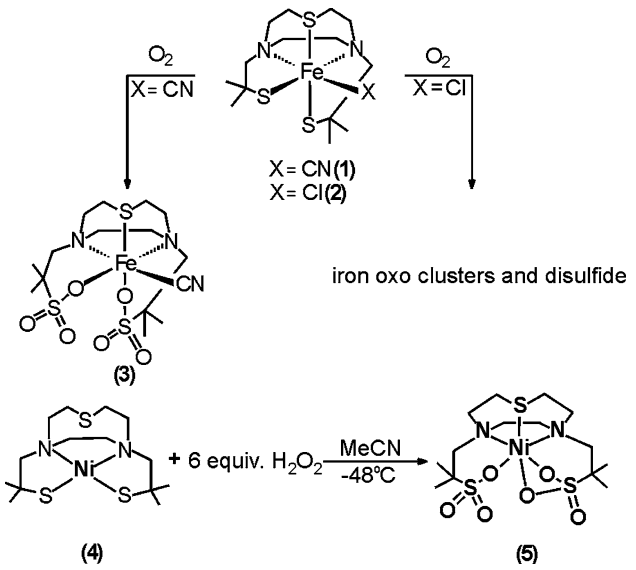

Scheme 1 Oxygenation pathways for **1**, **2**, and **4**

thiocyanate hydrolase is similar to that of NHase and also shows posttranslational oxygenation of active-site iron thiolates [27, 28].

Prior to the discovery of sulfur-oxygenated donors at the active site of NHase, it was generally established that oxygen exposure of iron(III) thiolates typically yields disulfide formation coupled with metal reduction and decomplexation of the ligand [3, 7, 34, 35]. Inspired by NHase, sulfur oxygenation of iron thiolates by dioxygen has been observed more recently [36–44]. In nearly all cases of sulfur oxygenation, a low-spin configuration for the iron thiolate precursor has been reported.

These results led us to investigate the spin-state dependency of iron thiolate oxygen sensitivity. We have previously shown that iron complexes of the pentadentate ligand 4,7-bis(2′-methyl-2′-mercaptopropyl)-1-thia-4,7-diazacyclononane), $(bmmp\text{-}TASN)^{2-}$, yield good spectroscopic models of the NHase active site [45–47]. Importantly, the spin state of iron in (bmmp-TASN)FeX complexes is a function of the exogenous donor, X, such that the effect of spin state on the oxygen sensitivity can be probed with only minor changes in the overall coordination sphere. In this paper, we report the oxygen sensitivity of the low-spin complex (bmmp-TASN)-FeCN (**1**) and its high-spin counterpart, (bmmp-TASN)FeCl (**2**) (Scheme 1). These experimental results are correlated with the covalency of the iron thiolate bond as determined by theoretical methods.

Materials and methods

Materials and techniques

All reagents and reactants were obtained from commercially available sources and were used as received unless otherwise noted. The iron complexes **1** and **2** were prepared as previously reported [46]. All solvents were dried and freshly distilled using standard techniques under a nitrogen atmosphere [48, 49]. Standard Schlenk techniques under an argon atmosphere or an argon-filled glove box were utilized for the manipulation of all compounds in this study [50].

Physical methods

Elemental analyses were performed by Midwest Microlab (Indianapolis, IN, USA) or Galbraith Laboratories (Knoxville, TN, USA). IR spectra were recorded using a Thermo Nicolet Avatar 360 spectrometer at 4-cm^{-1} resolution. Electronic absorption spectra were recorded with an Agilent 8453 diode array spectrometer with 1 cm path length quartz cells. Cyclic voltammetric measurements were performed using a PAR 273 potentiostat with a three-electrode cell (glassy carbon working electrode, platinum wire counter electrode, and Ag/AgCl reference electrode) at room temperature. Electrospray ionization (ESI) mass spectrometry (MS) was performed by the Laboratory for Biological Mass Spectrometry at Texas A&M University.

(4,7-Bis(2′-methyl-2′-sulfonatopropyl)-1-thia-4,7-diazacyclononane)iron(III) cyanide

A solution of 50 mg (0.13 mmol) of **1** in 50 mL dry methanol was purged with oxygen gas (after passing through a drying tube) for 5 min. The vessel was closed under an O_2 atmosphere and stirring of the solution continued for approximately 72 h, resulting in a color change of the solution from purple to blue and precipitation of crude 4,7-bis(2′-methyl-2′-sulfonatopropyl)-1-thia-4,7-diazacyclononane)iron(III) cyanide (**3**) as an olive-green

solid. Following evaporation of the solvent under vacuum, the crude product was washed with chloroform (2 × 30 mL), hexane (20 mL), and diethyl ether (20 mL) to yield purified **3**. Yield: 22 mg, 32% (based on the formula from elemental analysis). IR (KBr pellet; cm^{-1}): 2962 (br), 2913 (br), 2062 (s), 1580 (m), 1462 (m), 1356 (m), 1262 (w), 1221 (m), 1111 (s), 1021 (s), 947 (s), 800 (m), 477(s). MS-ESI, *m/z* calcd. for $C_{15}H_{28}N_3O_6S_3Fe{\cdot}K^+$, $[M + K^+]$ 537.01; found, 537.88. Three attempts to obtain elemental analysis for **3** were unsuccessful. While the results contained the correct ratio of carbon, hydrogen, and nitrogen the absolute values were lower than predicted. This is ascribed to the presence of additional insoluble products lacking carbon, hydrogen, or nitrogen, most likely an iron oxide. The "best" analysis assumed the presence of an impurity with an empirical formula of Fe_2O_3. Anal. calcd. for $C_{15}H_{28}N_3O_6S_3Fe{\cdot}0.20Fe_2O_3$: C, 33.97; H, 5.32; N, 7.92. Found: C, 33.58; H, 5.39; N, 7.74.

Oxygenation of **2**

Through a solution of 100 mg (0.24 mmol) of **2** in 100 mL dry methanol, oxygen gas was purged (after passing through a drying tube) for 5 min. The vessel was closed and the solution was stirred under an O_2 atmosphere for 24 h yielding a yellow-orange solution and an orange precipitate. Following evaporation of the solvent under vacuum, soluble products were extracted into chloroform (50 mL), leaving an iron-oxo cluster as an orange solid. The solid was further washed with 20-mL portions of chloroform, hexane, and diethyl ether. From the initial chloroform extract, the disulfide of H_2(bmmp-TASN), 3,3,6,6-tetramethyl-4,5,11-trithia-1,8-diazabicyclo[6.5.2]pentadecane (L_{SS}), was obtained by evaporation of the solvent and extraction into diethyl ether.

For iron-oxo clusters: yield: 40 mg, 76% (based on the empirical formula from elemental analysis). IR (KBr pellet; cm^{-1}): 2962 (br), 2913 (br), 2859 (w), 1491 (m), 1458 (m), 1375 (m), 1358 (m), 1309 (m), 1110 (m), 1051 (m), 652 (m), 460 (m). Although the molecular formula of the iron-oxo cluster(s) is unknown, the "best" empirical formula based on elemental analysis is $[H(L_{SS})][Fe_3O_3(OCH_3)_4]$. Anal. calcd. for $C_{18}H_{41}N_3O_7S_3Fe_3$: C, 32.70; H, 6.25; S, 14.55. Found: C, 33.77; H, 5.83; S, 14.28.

For L_{SS}: yield: 12 mg, 16%, ^{1}H NMR ($CDCl_3$): δ 3.1–3.2 (m, 6H), 2.5–2.8 (m, 10H), 1.2 (s, 12H). +ESI-MS, *m/z* calcd. for $C_{14}H_{29}N_2S_3$ $[M + H^+]$ 321.15; found, 321.14.

(4,7-Bis(2′-methyl-2′-mercaptopropyl)-1-thia-4,7-diazacyclononane)nickel(II)

To a solution of H_2(bmmp-TASN) (0.45 g, 1.4 mmol) in dry, degassed ethanol (10 mL) was added via a cannula a solution of KOH (0.16 g, 2.9 mmol) in 5 mL degassed ethanol. To the resulting cloudy mixture was added dropwise via a cannula a solution of $NiCl_2{\cdot}6H_2O$ (0.30 g, 1.3 mmol) in degassed ethanol (20 mL), resulting in an immediate color change to brown. The solution was stirred for 16 h and this was followed by solvent removal under vacuum. The residue was washed three times with diethyl ether and hot hexane. The resulting navy-green solid was dried under vacuum, yielding 4,7-bis(2′-methyl-2′-mercaptopropyl)-1-thia-4,7-diazacyclononane)nickel(II) (**4**) as a crude product. Single crystals suitable for X-ray crystallography were obtained by slow diffusion of ether into a methanol solution of **4**. Yield 0.20 g (0.53 mmol, 24%). Electronic absorption (acetonitrile): λ_{max} (ε): 279 (230), 400 (100), 479 (30). IR (KBr pellet, cm^{-1}): 3490 (br), 2966 (s), 2913 (s), 2847 (s), 1666 (m), 1454 (m), 1380 (w), 1172 (m), 1029 (m), 947 (m), 808 (w), 755 (w), 637 (w), 559 (w). +ESI-MS, *m/z* calcd. for $C_{14}H_{28}N_2S_3Ni$, [M+] 378.08; found, 378.07. Anal. calcd. for $C_{14}H_{28}N_2S_3Ni{\cdot}KCl$ C, 37.55; H, 6.22; S, 21.19. Found: C, 37.68; H, 6.23; S, 21.42.

(4,7-Bis(2′-methyl-2′-sulfonatopropyl)-1-thia-4,7-diazacyclononane)nickel(II)

A solution of **4** (50 mg, 0.13 mmol) in 50 mL freshly distilled acetonitrile was cooled to 258 K. To this was added a solution of 0.5 mL 30% hydrogen peroxide diluted in 20 mL acetonitrile. The mixture was kept cold and stirred for 2 h as the solution developed a light-blue color. After having been stirred overnight, solvent was removed in vacuo and the product was extracted into 5 mL methanol. Addition of 50 mL diethyl ether yielded purified (4,7-bis(2′-methyl-2′-sulfonatopropyl)-1-thia-4,7-diazacyclononane)nickel(II) (**5**) as a light-blue solid. Single crystals suitable for X-ray crystallography were grown through slow evaporation of a methanol solution of **5**. Yield: 30 mg (0.063 mmol, 48%). Electronic absorption (methanol): λ_{max} (ε): 266 (380), 307 (320), 623 (80). IR (KBr pellet; cm^{-1}): 2974 (br), 1458(m), 1258 (s), 1143 (s), 1106 (s), 1012 (s), 800 (w), and 694 (s). +ESI-MS, *m/z* calcd. for $C_{14}H_{28}N_2S_3O_6Ni$, $[M + H^+]$ 475.05; found, 475.05. Anal. calcd. for $C_{14}H_{28}N_2S_3O_6Ni{\cdot}KCl$ C, 30.58; H, 5.13; S, 17.49. Found: C, 29.82; H, 5.69; S, 17.65.

Isotopic labeling studies

Isotopic labeling studies with complexes **1** and **2** were conducted according to the protocols listed in the previous sections with the exception that the purge of $^{18}O_2$ through the solutions was conducted for 30 s instead of 5 min.

Crystallographic studies

For **1**, **4**, and **5** X-ray data were collected using a Bruker SMART APEX CCD diffractometer at 100 K using the SMART [51] software package (version 5.628) and were processed using SAINT [52] (version 6.36). Data were corrected for absorption using SADABS [53] (version 2.02) and the structures were solved using SHELXS-90 [54] refined by least-squares methods on F^2 using SHELXL-97 [54] incorporated into the SHELXTL [54] (version 6.12) suite of programs. Crystallographic parameters for each structure may be found in Table 1, with full details in the electronic supplementary information.

Theoretical method

Geometry optimizations and single-point-energy calculations were performed using the Gaussian 03 software package [55]. For geometry optimizations, the BP86 exchange–correlation functional was employed because of its successful prediction of geometries for numerous transition metal complexes [56–58]. For these calculations a 6-31g(d) basis set was found to produce results most consistent with experimentally determined geometries. This level of theory also successfully predicted the experimental ground-state spin state for complexes **1** and **2**. Single-point energies and molecular orbital coefficients were calculated using the B3LYP functional [59, 60]. A

Table 1 Crystal data and structure refinement for **1**, **4**, and **5**

Empirical formula	$C_{15}H_{28}FeN_3S_3$	$C_{14}H_{28}N_2NiS_3$	$C_{14}H_{28}N_2NiO_6S_3$
Formula weight	402.43	379.27	475.27
Temperature (K)	100(2)	100(2)	100(2)
Wavelength (Å)	0.71073	0.71073	0.71073
Crystal system	Monoclinic	Monoclinic	Triclinic
Space group	$P2_1/n$	$P2_1/n$	$P\bar{1}$
Unit cell dimensions			
a (Å)	$a = 7.2917$ (4)	$a = 7.5478$ (5)	$a = 11.3992$ (13)
b (Å)	$b = 19.3135$ (11)	$b = 11.9317$ (8)	$b = 12.3069$ (14)
c (Å)	$c = 12.8168$ (8)	$c = 18.7230$ (12)	$c = 14.8854$ (17)
α (°)			89.098(2)
β (°)	100.3160 (10)	93.3250 (10)	76.068 (2)
γ (°)			80.096 (2)
Volume (Å^3)	1,775.79 (18)	1,683.32 (19)	1,995.9 (4)
Z	4	4	4
Density (Mg/m^3) (calcd.)	1.505	1.497	1.582
Absorption coefficient (mm^{-1})	1.202	1.517	1.318
Crystal size (mm^3)	0.38 × 0.10 × 0.08	0.12 × 0.10 × 0.01	0.21 × 0.18 × 0.04
θ range for data collection (°)	1.93–28.10	2.02–28.30	1.68–28.07
Index ranges	$-9 \le h \le 9$	$-9 \le h \le 9$	$-14 \le h \le 15$
	$-24 \le k \le 25$	$-15 \le k \le 15$	$-15 \le k \le 15$
	$-16 \le l \le 16$	$-24 \le l \le 24$	$-19 \le l \le 19$
Reflections collected	15,368	14,831	17,502
Independent reflections	4,137 ($R_{int} = 0.0267$)	4,000 ($R_{int} = 0.0448$)	8,873 ($R_{int} = 0.0250$]
Completeness	95.70% ($\theta = 28.10°$)	95.80% ($\theta = 28.30°$)	91.40% ($\theta = 28.07°$)
Absorption correction	SADABS	SADABS	SADABS
Refinement methods	Full-matrix least-squares on F^2		
Data/restraints/parameters	4,137/15/232	4,000/0/185	8,873/0/477
Goodness of fit on F^2	1.056	1.054	1.065
Final R indices [$I > 2\sigma(I)$][a]	$R_1 = 0.0392$, $wR_2 = 0.0899$	$R_1 = 0.0413$, $wR_2 = 0.0759$	$R_1 = 0.0754$, $wR_2 = 0.1573$
R indices (all data[a])	$R_1 = 0.0474$, $wR_2 = 0.0933$	$R_1 = 0.0555$, $wR_2 = 0.0800$	$R_1 = 0.0844$, $wR_2 = 0.1618$
Largest peak and hole (e^- Å^{-3})	0.521 and −0.426	0.512 and −0.380	2.091 and −1.341

[a] $R_1 = \Sigma||F_0| - |F_c||/\Sigma|F_0|$, $wR_2 = \{\Sigma[w(F_0^2 - F_c^2)^2]/\Sigma[w(F_0^2)^2]\}^{1/2}$

mixed basis set [LanL2DZ for Fe, 6-311g(d, p) for S and Cl, and 6-31g(d) for C, H, and N] was employed. All single-point-energy calculations were converged to a tight RMS threshold of 1×10^{-8}. The results were examined for spin contamination by comparing the term $(4\ \langle S^2\rangle_{\mathrm{UHF}} + 1)^{-1/2}$ with the expected spin multiplicity [61]. In all cases, spin contamination was found to be nonexistent or negligible. Partial charges and spin densities were derived from a natural population analysis. Natural bond order (NBO) calculations were performed using NBO 5.0 as implemented within Gaussian 98 [62, 63]. Molecular orbitals were visualized from cube files using the VMD software package [64]. Publication-quality images were rendered using Pov-Ray version 3.6 [65]. The NBO orbitals were visualized as 2D contour plots using NBOview 1.0 [62], and as 3D representations using Molekel version 4.3 [66].

Results

Synthesis and spectroscopy

The synthesis of the low-spin iron complex **1** from **2** and $[NEt_4][CN]$ was described previously [46]. Conductivity experiments revealed that **1** is a nonelectrolyte in solution, indicating the cyanide donor remains bound in solution. Complex **1** is stable in air as a solid and under an argon atmosphere in solution. When dioxygen is purged through a methanol solution of **1** the initial dark-purple color is retained for several hours. However, when it is stirred under an O_2 atmosphere the solution develops a distinct blue color over several days (3–7 days), from which (cyanato)(4,7-bis(2′-methyl-2′-sulfonatopropyl)-1-thia-4,7-diazacyclononane)iron(III) precipitates as a dark-green solid (**3**). The IR spectrum of **3** displays a C≡N asymmetric stretch at 2062 cm^{-1}, which is redshifted with respect to that of the dithiolate precursor **1**, 2083 cm^{-1} (Fig. 2, spectrum A) [46]. Additionally, **3** displays characteristic peaks at 1221, 1111, 1021, 947, 800, and 477 cm^{-1}. The intensity and frequency of these peaks are consistent with metal-coordinated sulfur-oxygenates [67–69]. Isotopic labeling experiments with $^{18}O_2$ resulted in a shift of the bands at 1221, 947, and 477 cm^{-1} to 1203, 922, and 460 cm^{-1}, respectively. These shifts of 17–25 cm^{-1} are consistent with incorporation of ^{18}O (Fig. S1) [70]. Prolonged oxygen exposure (several weeks) of **3** in the presence of solvent yields an uncharacterized orange compound.

Complex **3** is insoluble in all common laboratory solvents, precluding complete solution characterization. Trace quantities of **3** were extracted into methanol for analysis by MS in the presence of K^+, which has been shown to enhance ionization of nickel sulfur-oxygenates [70]. The +ESI-MS displays the expected $[M + K^+]$ peak at *m/z* 537.88 (Fig. S2).

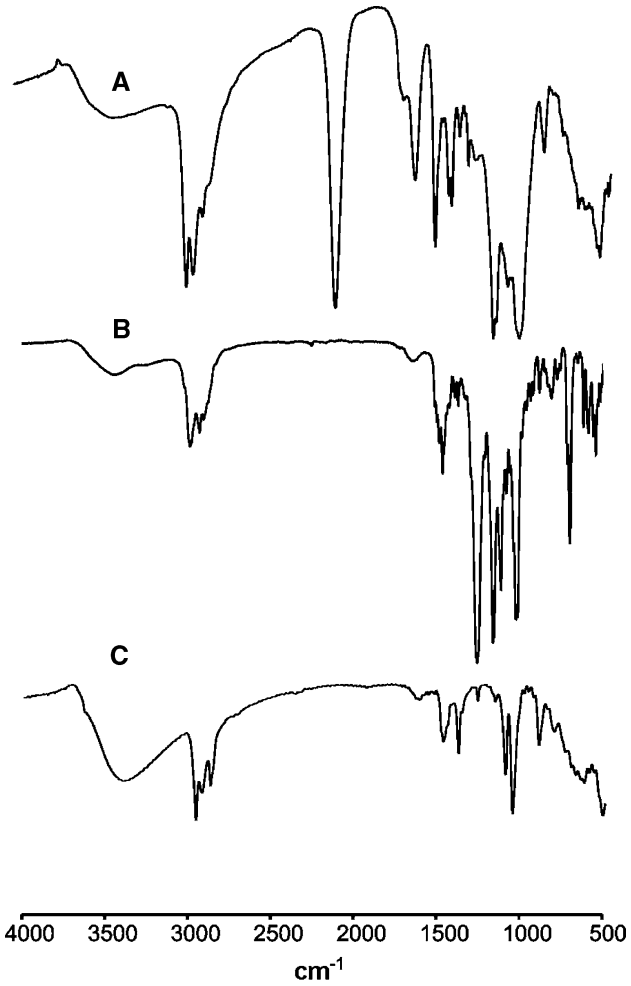

Fig. 2 *A* IR spectrum of **3**. *B* IR spectrum of **5**. *C* IR spectrum of $[Bu_4N][Fe_{14}O_8(CH_3CH_2O)_{20}Cl_8]$ [76]

Since the insolubility of **3** hampered efforts to obtain single crystals for X-ray characterization, the nickel analogues of **1** and **3** were prepared. The nickel dithiolate [(bmmp-TASN)Ni] (**4**) was synthesized from the dropwise addition of an ethanol solution of $NiCl_2{\cdot}6H_2O$ to an ethanol solution containing H_2(bmmp-TASN) and KOH. The olive-green complex **4** is soluble in several organic solvents (including alcohols, chloroform, and acetonitrile) and is stable towards O_2 as a solid and in solution. Compound **4** reacts rapidly with hydrogen peroxide in acetonitrile to produce the nickel-containing disulfonate **5** as a light-blue solid. To ensure complete conversion of **4** to **5**, an excess of hydrogen peroxide was employed. The IR spectrum of **5** (Fig. 2, spectrum B), is dominated by the presence of very intense sharp bands at 1258, 1143, 1106, 1012, 800, and 694 cm^{-1}. These bands are similar to those of **3**, suggesting the complexes share similar ligand environments.

The high-spin iron complex **2** is air-stable in the solid state and exhibits long-term stability in anaerobic solutions. In oxygen-saturated solutions, **2** rapidly (1 h) changes color from dark blue to yellow, with precipitation of an orange iron-oxo product. The orange product displays an IR spectrum with weak to medium intensity bands at 1309, 1110, 1051, 895, 652, and 460 cm^{-1} (Fig. 2, spectrum C). Although some of these bands are in the region expected for sulfur-oxygenates, the intensities are too weak and the energies do not shift when the complex is prepared using $^{18}O_2$. The bands are therefore attributed to methoxide, which also displays features in this region [71]. In fact, the IR spectrum of the orange iron-oxo product is nearly identical to that of the previously reported cluster $[Bu_4N][Fe_{14}O_8(CH_3CH_2O)_{20}Cl_8]$, which was also isolated as an orange solid upon oxygenation of a related precursor [72]. Although the cluster was not amenable to mass-spectral analysis, L_{SS} was extracted from the crude reaction product into chloroform. The +ESI-MS of L_{SS} displays a peak at $m/z = 321.14$ consistent with that of the expected intramolecular disulfide; $m/z = 321.15$ (Fig. S3). These results indicate that unlike **1**, **2** does not react with O_2 to yield iron sulfur-oxygenates, but rather decomposes to disulfide and iron-oxo clusters.

Structural characterization

Single crystals of **1** suitable for X-ray diffraction studies were obtained through slow evaporation of an acetonitrile solution of **1** under an argon atmosphere. An ORTEP representation of **1** is shown in Fig. 3, and selected bond distances and angles are displayed in Table 2 [73]. The iron atom resides in a pseudo-octahedral N_2S_3C donor environment. The TASN ring (N1, N2, S1) occupies one face of the octahedron, while the pendant thiolate donors S2 and S3 are located *trans* to S1 and N1, respectively. The same arrangement is found in the structures of $[(bmmp\text{-}TASN)Fe(NO)]^+$ and $[(bmmp\text{-}TASN)Fe]_2O$ [46]. The cyanide ligand resides *trans* to N2. The Fe–$S_{thiolate}$ bond distances of 2.311(4) and 2.179(4) Å are within the expected range for low-spin iron complexes containing similar donor sets [46, 74–78]. The Fe–$S_{thioether}$ bond distance is intermediate between the two Fe–$S_{thiolate}$ bond distances, consistent with previous observations that thioethers and thiolates are structurally similar in low-spin iron complexes [45]. Interestingly, the distance of the thiolate sulfur, S2, *trans* to the thioether S1 is significantly longer than that of the thiolate sulfur, S3, *trans* to the amine N1. The cyano group is bound to iron via a carbon atom in a nearly linear fashion with an N3–C15–Fe bond angle of 177.4(16)°. Of additional note, the five-member NS chelate rings containing N1/S2 and N2/S3 are nearly perpendicular with an angle of 84.0° between the planes. Since the sulfur

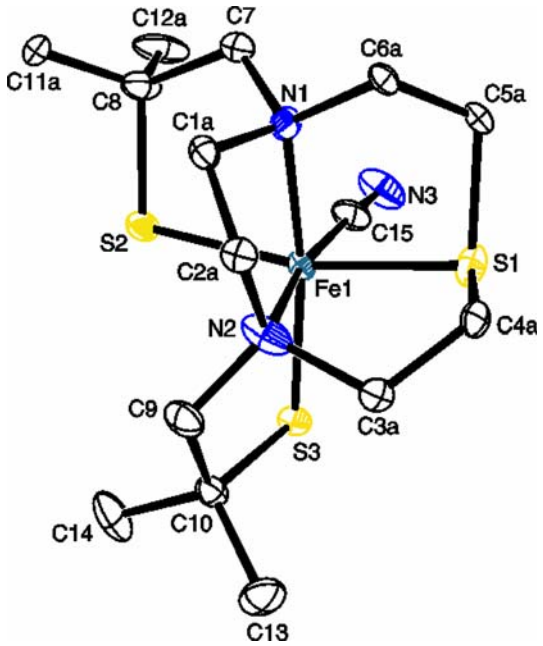

Fig. 3 ORTEP [78] view of **1** showing 50% probability displacement ellipsoids and atom-numbering scheme. Hydrogen atoms are omitted

Table 2 Selected bond distances (Å) and bond angles (°) for **1**

Fe–S1	2.286(4)	Fe–N1	2.069(11)
Fe–S2	2.311(4)	Fe–N2	2.078(12)
Fe–S3	2.179(4)	Fe–C15	1.922(15)
N1–Fe–N2	83.7(5)	N2–Fe–S1	86.0(4)
N1–Fe–S1	86.8(3)	N2–Fe–S3	85.4(4)
N1–Fe–S2	83.2(3)	S2–Fe–S3	93.24(14)
C15–Fe–S2	87.8(5)	N3–C15–Fe	177.4(16)

p-type lone pair of electrons lie orthogonal to its respective chelate ring, the thiolate lone pairs also lie in nearly perpendicular orbitals with significant electronic ramifications (vida infra).

Single crystals of (bmmp-TASN)Ni were obtained through slow vapor diffusion of diethyl ether into a methanol solution of **4**. An ORTEP representation of **4** is shown in Fig. 4, with representative bond distances and angles presented in Table 3. The nickel center resides in a square-planar environment with an N_2S_2 donor set. The Ni–$S_{thiolate}$ and Ni–N distances are within the expected ranges for similar square-planar NiN_2S_2 complexes [79–81]. The thioether sulfur of the TASN backbone is perched in an axial position out of bonding range 2.824 Å away from the nickel, which is significantly greater than the sum of the van der Waal radii, 2.43 Å.

Single crystals of (bmmp-O_6-TASN)Ni were obtained through slow evaporation of a methanol solution of **5**. Examination of the ORTEP representation of **5** (Fig. 5)

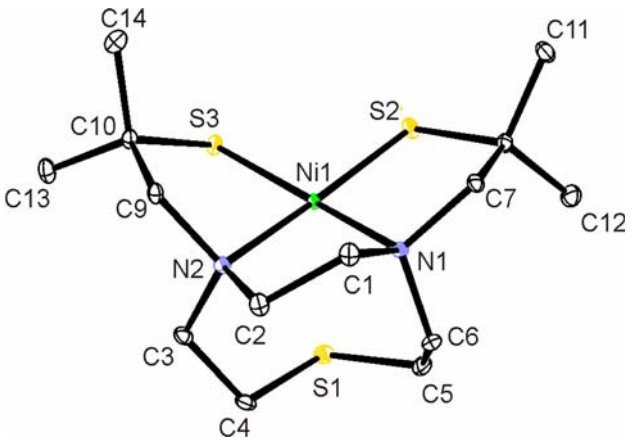

Fig. 4 ORTEP [78] view of **4** showing 50% probability displacement ellipsoids and atom-numbering scheme. Hydrogen atoms are omitted

Table 3 Selected bond distances (Å) and bond angles (°) for **4**

Ni–N1	1.957(2)	Ni–S2	2.1775(7)
Ni–N2	1.982(2)	Ni–S3	2.1925(7)
N1–Ni–N2	87.16(8)	N1–Ni–S2	90.02(6)
N2–Ni–S2	173.93(6)	N1–Ni–S3	170.96(6)
N2–Ni–S3	87.07(6)	S2–Ni–S3	95.05(3)

reveals the thiolate donors of **4** have been oxygenated to sulfonates. The nickel center resides in a pseudo-octahedral coordination sphere with a donor set consisting of the amine donors N1 and N2, the thioether sulfur S1, the η^1 sulfonate donor O1, and the η^2 sulfonate donors O2 and O3. Bond distances and angles are summarized in Table 4.

Computational studies

Spin-unrestricted geometry optimizations of complexes **1** and **2** were performed using the BP86 functional with the 6-31g(d) basis set. Initial coordinates for non-hydrogen atoms of **1** and **2** were taken from the crystallographic coordinates of $[(bmmp\text{-}TASN)FeNO]^+$ with substitution of NO by CN or Cl, respectively [45]. The standard orientations were adjusted to give Cartesian axes oriented along metal–ligand bonds, with the *z*-axis concomitant with the variable coordination site, and S1–Fe–S2 along the *y*-axis (Fig. 6). Energy and geometry optimizations with three possible spin states ($s = 1/2, 3/2, 5/2$) were performed for each complex, and the results are summarized in Table S1. For both complexes, the lowest-energy spin state is consistent with experimental observations. The quartet and sextet spin states of **1** lie 20.9 and 46.7 kcal/mol higher in energy than the ground-state doublet. For **2**, the sextet ground state is 10.6 and 19.9 kcal/mol lower in energy than the quartet and doublet spin states, respectively. The calculated metal–ligand bond distances are within 0.07 Å

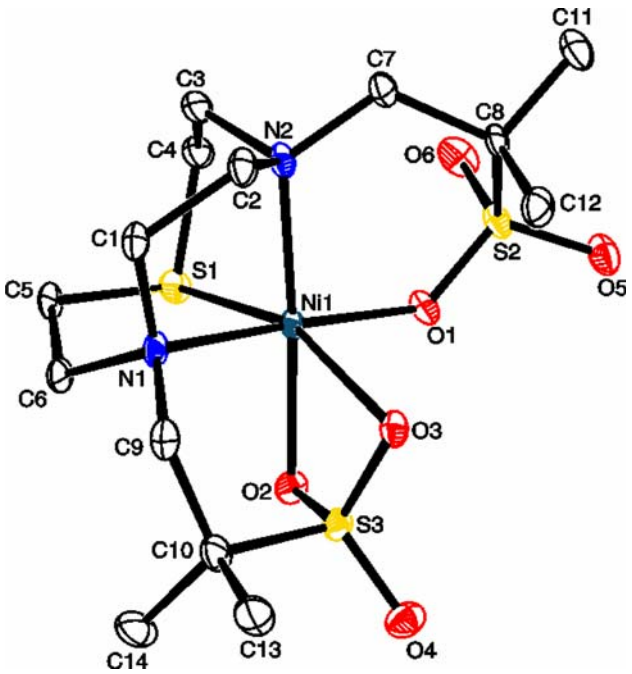

Fig. 5 ORTEP [78] view of **5** showing 50% probability displacement ellipsoids and atom-numbering scheme. Hydrogen atoms are omitted

Table 4 Selected bond distances (Å) and bond angles (°) for **5**

Ni–O1	1.991(4)	Ni–N1	2.103(4)
Ni–O2	2.134(4)	Ni–N2	2.139(5)
Ni–O3	2.283(4)	Ni–S1	2.3487(14)
N1–Ni–O1	173.25(16)	N2–Ni–O3	113.30(15)
N1–Ni–N2	85.98(17)	O2–Ni–O3	65.15(13)
N2–Ni–O2	174.18(16)	S1–Ni–O2	93.99(10)
N1–Ni–O3	85.68(15)	S1–Ni–O3	158.63(10)

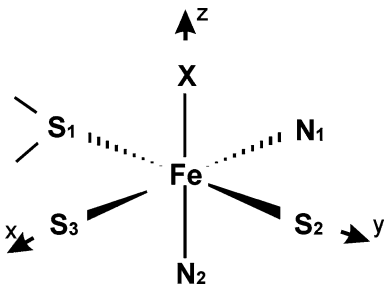

Fig. 6 Cartesian axes assigned for visualization of molecular orbitals for complexes **1** and **2**

of experimentally measured distances (Table S2). Single-point-energy calculations for the optimized structures of **1**, as a doublet, and **2**, as a sextet, were computed using the B3LYP functional, which has been shown to reliably determine the electronic structure of transition metal complexes [82]. As shown below, analyses of these results

reveal several key differences between **1** and **2** that influence their reactivity with dioxygen.

Complexes **1** and **2** each contain a formal iron(III) ion in a neutral complex: however, the partial charge distribution, as derived from a natural population analysis (Table 5), varies significantly between the complexes. The low-spin complex **1** has a small, positive charge on iron of +0.16, while in the high-spin complex **2**, the iron has a much larger partial charge of +1.09. The greater nephalauxetic effect [83] in **1** than in **2** results from changes in metal–sulfur bonding and changes in donor type in the variable position. The magnitude of the charge on the thiolate sulfur donors S2 and S3, −0.17 and −0.02, is significantly smaller in **1** than in **2**, −0.31 and −0.28. This is consistent with a greater sharing of electron density, more covalency, between iron and sulfur in the former. The greater Fe–$S_{thioether}$ interaction in **1** than in **2** yields partial charges on S1 of +0.40 and +0.24, respectively, owing to the increased sulfonium character in **1**. Additional decreases in the partial charge on iron in **1**, compared with **2**, are attributable to differences in the sixth ligand. The cyanide donor in **1** has an overall lower charge, −0.43, than the chloride in **2**, −0.59, consistent with the stronger σ-donor ability, and π-backbonding capabilities, of cyanide versus chloride.

While the charge distributions of **1** and **2** reveal significant differences in metal–ligand bonding, better insight into complex reactivity can be obtained through examination of the spin density (Table 5). For both **1** and **2**, the metal center and the primary coordination sphere account for more than 95% of the total spin density. In **1**, essentially all of the spin is localized on the iron ($0.806e^-$) and the thiolate sulfur S3 ($0.213e^-$). As shown in Fig. 7 (left), the spin residing on iron is localized within the angular constraints of a d_{xy} orbital, while the density about sulfur is within the angular boundaries of a p_y orbital. These results are consistent with earlier electron paramagnetic resonance results for which a g-value analysis, using the method of Taylor and Griffith, revealed more that 99% of the unpaired electron density in **1** resides in the d_{xy} orbital [46, 84, 85]. For complex **2**, in addition to the spin density on iron of $3.600e^-$, there is also a significant buildup of spin on both thiolate sulfurs ($0.405e^-$ and $0.435e^-$) for S2 and S3, respectively, and the chloride ($0.255\ e^-$). As shown in Fig. 7 (right), the spin density on iron is nearly spherically distributed as expected for high-spin iron(III). As a result, spin delocalization pathways are available for all the ligands bearing p-type lone-pair orbitals. The results of the spin-density calculations agree with the experimental electron paramagnetic resonance spectra of **2**, which depicts a high-spin iron center residing in a rhombic coordination environment [46, 86].

Table 5 Partial charges and spin distribution for complexes **1** and **2** from density functional theory (B3LYP)

Complex	Spin state	Atom	Partial charge	Spin density
1	1/2	Fe	0.16	0.806
		S1	0.40	−0.001
		S2	−0.17	0.013
		S3	−0.02	0.213
		N1	−0.47	−0.006
		N2	−0.50	−0.006
		N3	−0.50	0.010
		C15	0.07	−0.027
2	5/2	Fe	1.09	3.600
		S1	0.24	0.098
		S2	−0.31	0.405
		S3	−0.28	0.435
		N1	−0.55	0.086
		N2	−0.55	0.084
		Cl	−0.59	0.255

The Kohn–Sham frontier molecular orbitals for complexes **1** and **2**, as shown in Fig. 8 and summarized in Table S3, are as expected for low-spin and high-spin iron(III) complexes, respectively. For **1**, the unoccupied α-orbitals, 108α and 109α, and their β-orbital counterparts are the typical $d_{x^2-y^2}$ and d_{z^2} σ^* orbitals expected for low-spin iron(III). The three highest-energy occupied α-orbitals largely comprise π^* interactions between d_{yz} and S2 p_z, d_{xy} and S3 p_y, and d_{xz} and CN. In the β-orbitals, only the d_{yz}/S2 p_z and d_{xz}/CN counterparts are occupied, leaving the d_{xy}/S3 p_y π^* orbital being the location of the unpaired electron. This is consistent with the spin-density calculations.

The frontier molecular orbitals of **2** are qualitatively similar to those of **1**. The β-orbitals 107β–111β correspond to the same five orbitals described for **1**, with slightly different ordering and substitution of Cl for CN. The α-orbitals are more ligand-centered and not as easily visualized. The main quantitative difference between **1** and **2** is the lessened σ-donor ability and π-donor nature of Cl compared with CN. This has a pronounced effect on the relative energies of the frontier orbitals. Whereas the frontier orbitals for **1** span an average energy range of

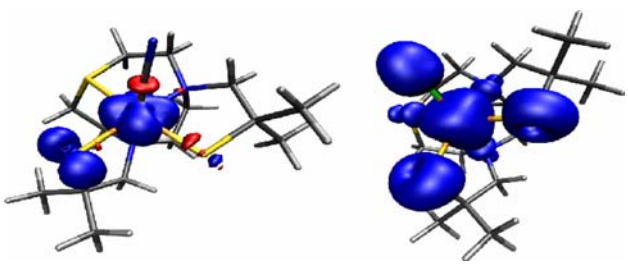

Fig. 7 Spin density for complexes **1** (*left*) and **2** (*right*)

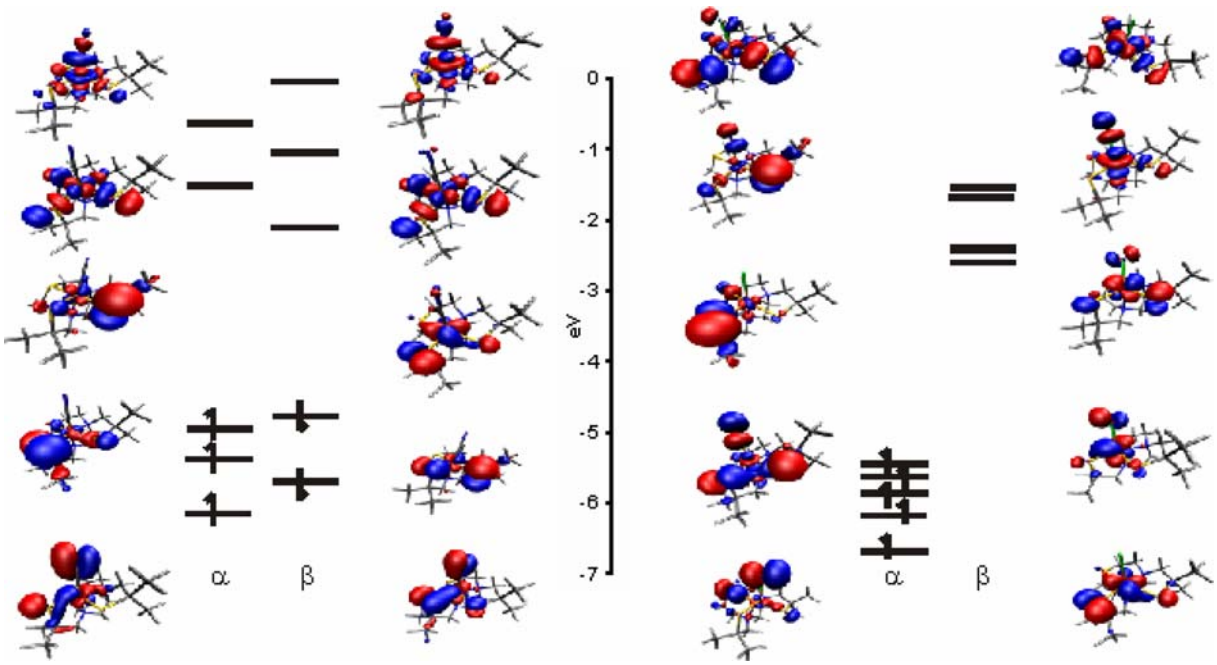

Fig. 8 Frontier molecular orbitals for **1** (*left*) and **2** (*right*)

5.59 eV, the gap between the highest and lowest frontier orbitals of **2** is only 1.2 eV. The weak σ-donor ability of the chloro group also causes the $\sigma * -d_{z_2}$ orbital to drop in energy relative to the $d_{x^2-y^2}$ orbital. Overall, the relative contributions to each molecular orbital from individual atoms do not clearly explain the spin-state dependence of dioxygen reactivity. For example, the five frontier α-orbitals for **1** have an average iron contribution of 50.74% and an average combined thiolate contribution of 13.38%. An analogous decomposition for **2** reveals 40.69 and 13.55% for iron and the thiolates, respectively.

While the Kohn–Sham molecular orbitals described above are consistent with the difference in spin state for complexes **1** and **2**, they provide little insight into how this influences reactivity. To probe further the differences in metal–sulfur bonding intimated by the partial charges, a covalency analysis was conducted using the NBO/natural localized molecular orbital (NLMO) protocol previously described by Boone et al. [61, 83] as a measure of relative covalency in iron-containing complexes.

A visualization of the Lewis-type structures computed by the NBO algorithm for **1** and **2** is shown in Fig. 9. Since the bonding contributions for the α- and β-orbitals are determined independently, an overall view of each bond requires a combination of both results. In Fig. 9, a solid line indicates a traditional two center–two electron bond, an arrow represents a ligand-centered lone pair that is partially donated to the metal but does not meet the NBO criteria for a covalent bond, and a half-arrow represents a partially covalent bond, which is defined as a traditional

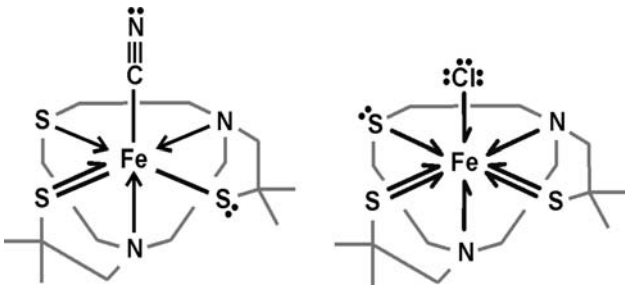

Fig. 9 Natural bond order determined Lewis structures for **1** (*left*) and **2** (*right*). See the text for the description of the arrow conventions

bond in the α-orbital, but as a lone-pair electron in the β-orbital (or vice versa).

In complex **1**, the two thiolate donors, S2 and S3, and the carbon of cyanide form traditional two center–two electron bonds with iron. In addition to σ-bonding, a partially covalent π bond between S3 and iron is assigned. The two nitrogen donors and the thioether sulfur (S1) contain lone pairs of electrons that are much less donating to the iron. In **2**, there are no traditional two center–two electron bonds between the ligands and iron. Each of the ligands is considered to have a partially covalent σ bond and the two thiolate sulfurs also have a partially covalent π bond. This is not unexpected, as all of the ligand-donor α-orbitals and metal-centered α-orbitals for this d^5 high-spin center are occupied. These results qualitatively confirm the notion that Fe–S bonding is more covalent in **1** than in **2**, but the results cannot be compared quantitatively since the criteria

for assigning bonds in NBO are variable and dependent on the best Lewis structure.

To directly compare the bonding of **1** and **2**, additional interactions need to be considered using NBO/NLMO as described by Boone et al. [61, 83]. This approach involves the summation of covalency contributions to metal–ligand bonding from three sources. These include traditional two center–two electron NBOs as assigned by the NBO algorithm, metal- and ligand-lone pair delocalizations as presented by NLMO analysis, and three center–four electron hyperbonding, which involves resonance stabilization between the metal center and *trans* donor atoms. Antibonding NBO/NLMO interactions are subtracted to yield an overall covalency for each metal–ligand bond. A value of 1.0 signifies a completely covalent interaction, while a value of 0.0 represents a completely ionic interaction.

Table 6 summarizes the covalency analysis for **1** and **2**, with the total covalency defined as the sum of the covalency of individual metal–ligand bonds. The total covalency of **1** ($3.73e^-$) is consistent with that of other low-spin iron thiolates analyzed by Boone et al. [61, 83]. The high-spin complex **2** displays a significantly lower total covalency of $1.30e^-$, which is in agreement with that of other high-spin iron complexes. Of particular interest is the covalency of the iron–thiolate bonds. For the Fe–S2 bond, significantly greater covalency is observed in **1** ($0.75e^-$) than in **2** ($0.11e^-$). A similar trend is observed for the Fe–S3 bond, with values of $0.86e^-$ and $0.40e^-$ for **1** and **2**, respectively. The greater covalency of **1** is partially attributable to three-center hyperbonding with the *trans* ligands. This is further evident by the high degree of covalency in the iron–ligand bonds to the thioether sulfur S1 ($0.84e^-$) and the amino nitrogen N2 ($0.58e^-$) which are *trans* to the thiolates S2 and S3, respectively. No hyperbonding interactions were detected in **2**.

Table 6 Covalency values for complexes **1** and **2** calculated from natural bond order/natural localization molecular orbital analysis

Bond	Bond covalency ($\|e^-\|$)	Total covalency ($\|e^-\|$)
1		
Fe–S1	0.84	3.73
Fe–S2	0.75	
Fe–S3	0.86	
Fe–N1	0.13	
Fe–N2	0.58	
Fe–C15	0.56	
2		
Fe–S1	0.32	1.30
Fe–S2	0.11	
Fe–S3	0.40	
Fe–N1	0.08	
Fe–N2	0.10	
Fe–Cl	0.29	

Discussion

Using the pentadentate ligand $(bmmp\text{-}TASN)^{2-}$ to provide a consistent iron dithiolate core, the oxygen sensitivity of two closely related iron dithiolate complexes with dioxygen has revealed an intriguing spin-state dependence. The low-spin derivative, **1**, demonstrates sulfur-centered oxygenation to yield an isolable iron disulfonate, **3**. In contrast, upon exposure to dioxygen, the high-spin derivative, **2**, decomposes to disulfide and an iron-oxo cluster. These results provide insight into the vexing problem of iron thiolate oxygen sensitivity.

Prior to the discovery of dioxygen-induced sulfur oxygenation of iron thiolates at the active site of NHase, the dioxygen reactivity of iron thiolates was largely limited to disulfide formation and complex degradation. Interestingly, these earlier complexes were by and large high-spin, consistent with the weak-field donor ability of thiolates. However, since the elucidation of the NHase active site, efforts to generate low-spin iron thiolates and iron-coordinated sulfur oxygenates have increased, although direct dioxygen addition to iron thiolates has been limited [36–43]. Additionally, the prevalence of iron–thiolate bonds in both naturally occurring and synthetic systems necessitates an understanding of the parameters influencing their dioxygen reactivity.

Our approach to understanding the apparent spin-state dependence of the reactivity of iron thiolates with dioxygen centers on differences in the covalency of the Fe–S bonds as a function of spin state. As shown in the current study with **1** and **2**, and in prior studies of iron thiolates, the low-spin state yields significantly covalent Fe–S bonds, while the high-spin state gives a more ionic Fe–S bond. This observation provides significant insight into the reactivity of the Fe–S–R moiety.

For ionic iron–thiolate bonds, the thiolate sulfur maintains a significant negative charge and the moiety is akin to a simple thiolate salt, such as NaSR. Like simple thiolate salts, oxygen exposure is expected to yield disulfides (Scheme 2) [7, 87, 88]. However, when the Fe–S bond is

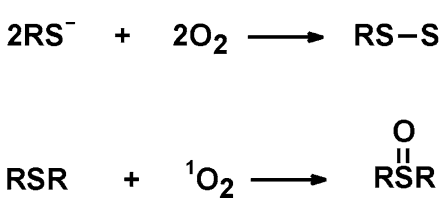

Scheme 2 Oxygenation pathways for RS^- and RSR

covalent, the moiety is akin to an organic sulfide, R′SR. The iron can be viewed as an electron-donating R′ since the bond is polarized towards sulfur, which maintains a small, negative partial charge. In this case, the Fe–S–R moiety, like organic sulfides, follows a pathway to sulfur oxygenation (Scheme 2) [89, 90].

In addition to covalency considerations, the doublet ground state of **1**, with significant spin density on the thiolate sulfur S3, promotes the reaction with triplet ground state dioxygen and the reaction proceeds rapidly. This is in contrast to organic sulfides, which have a singlet ground state and require excitation of oxygen to the singlet state for oxygenation [67, 89, 90]. Consistent with these observations, we previously reported that sulfur oxygenation of a singlet ruthenium(II) thiolate proceeds via a metal-centered oxidation by O_2 to generate a reactive doublet ruthenium(III) thiolate complex, which only then reacts with triplet dioxygen to yield the sulfur-oxygenated product [91].

With regards to NHase, the current study provides insight into the sulfur-oxygenation process. It is evident that the spin state of iron has dramatic effects on sulfur-based reactivity of iron thiolates. The low-spin state imparts Fe–S bond covalency that favors sulfur oxygenation, paralleling organic sulfides. Although low-spin iron(II) and iron(III) meet this criterion, iron(II) has a singlet ground state for which the reaction with ground-state, triplet oxygen would be spin-forbidden. As such, only low-spin iron(III) thiolates are expected to display rapid oxygen reactivity leading to sulfur-oxygenated product. Previous model complexes of the iron-containing NHase employing thiolate sulfur and deprotonated amide donors have been found to posses exclusively a low-spin ground state [6, 7, 42]. Computational studies on the NHase active site as well as small-molecule mimics have shown that amides *trans* to thiolates in these complexes were found to participate in three-center hyperbonding, as does **1** [61, 83]. This implies that the active site of NHase most likely contains low-spin iron(III) prior to sulfur oxygenation. Although the mechanism by which the active site is posttranslationally modified remains unknown, it has become clear that the low-spin state of the active site will favor the formation of sulfur oxygenates rather than disulfide formation. The spin-state-dependent reactivity pattern found in complexes **1** and **2** may also be applicable to other Fe–S systems, particularly when such systems are to be subjected to some form of oxidative stress as can be found in certain physiological circumstances or in industrial processes requiring robust catalysts [92].

Acknowledgments We wish to acknowledge Donald DuPré, Lucius Johnson, Jessica Koehler, and Jadwiga Kuta for assistance with the computational work. This work was supported by the National Science Foundation (CHE-0238137).

References

1. Momenteau M, Reed CA (1994) Chem Rev 94:659–698
2. Denisov IG, Makris TM, Sligar SG, Schlichting I (2005) Chem Rev 105:2253–2277
3. Holm RH (1977) Acc Chem Res 10:427–434
4. Beinert H, Holm RH, Munck E (1997) Science 277:653–659
5. Kovacs JA (2004) Chem Rev 104:825–848
6. Harrop TC, Mascharak PK (2004) Acc Chem Res 37:253–260
7. Mascharak PK (2002) Coord Chem Rev 225:201–214
8. Kovacs JA, Brines LM (2007) Acc Chem Res 40:501–509
9. Droge W, Schipper HM (2007) Aging Cell 6:361–370
10. Szacilowski K, Chmura A, Stasicka Z (2005) Coord Chem Rev 249:2408–2436
11. Dey A, Jenney FE, Adams MWW, Johnson MK, Hodgson KO, Hedman B, Solomon EI (2007) J Am Chem Soc 129:12418–12431
12. Kitagawa T, Dey A, Lugo-Mas P, Benedict JB, Kaminsky W, Solomon E, Kovacs JA (2006) J Am Chem Soc 128:14448–14449
13. Dey A, Hocking RK, Larsen P, Borovik AS, Hodgson KO, Hedman B, Solomon EI (2006) J Am Chem Soc 128:9825–9833
14. Lugo-Mas P, Dey A, Xu L, Davin SD, Benedict J, Kaminsky W, Hodgson KO, Hedman B, Solomon EI, Kovacs JA (2006) J Am Chem Soc 128:11211–11221
15. Solomon EI, Gorelsky SI, Dey A (2006) J Comput Chem 27:1415–1428
16. Dey A, Hocking RK, Larsen P, Borovik AS, Hodgson KO, Hedman B, Solomon EI (2006) J Am Chem Soc 128:9825–9833
17. Dey A, Chow M, Taniguchi K, Lugo-Mas P, Davin S, Maeda M, Kovacs JA, Odaka M, Hodgson KO, Hedman B, Solomon EI (2006) J Am Chem Soc 128:533–541
18. Dey A, Roche CL, Walters MA, Hodgson KO, Hedman B, Solomon EI (2005) Inorg Chem 44:8349–8354
19. Solomon EI, Hedman B, Hodgson KO, Dey A, Szilagyi RK (2005) Coord Chem Rev 249:97–129
20. Dey A, Glaser T, Moura JJG, Holm RH, Hedman B, Hodgson KO, Solomon EI (2004) J Am Chem Soc 126:16868–16878
21. Dey A, Glaser T, Couture MMJ, Eltis LD, Holm RH, Hedman B, Hodgson KO, Solomon EI (2004) J Am Chem Soc 126:8320–8328
22. Dey A, Okamura T, Ueyama N, Hedman B, Hodgson KO, Solomon EI (2005) J Am Chem Soc 127:12046–12053
23. Stiefel EI, Matsumoto K (1996) Transition metal sulfur chemistry: biological and industrial significance and key trends. American Chemical Society, Washington, DC
24. Costas M, Mehn MP, Jensen MP, Que L (2004) Chem Rev 104:939–986
25. Hausinger RP (2004) Crit Rev Biochem Mol Biol 39:21–68
26. Kappock TJ, Caradonna JP (1996) Chem Rev 96:2659–2756
27. Arakawa T, Kawano Y, Kataoka S, Katayama Y, Kamiya N, Yohda M, Odaka M (2007) J Mol Biol 366:1497–1509
28. Katayama Y, Hashimoto K, Nakayama H, Mino H, Nojiri M, Ono T, Nyunoya H, Yohda M, Takio K, Odaka M (2006) J Am Chem Soc 128:728–729
29. Sugiura Y, Kuwahara J, Nagasawa T, Yamada H (1987) J Am Chem Soc 109:5848–5850
30. Shigehiro S, Nakasako M, Dohmae N, Tsujimura M, Tokoi K, Odaka M, Yohda M, Kamiya N, Endo I (1998) Nat Struct Biol 5:347–351
31. Lu J, Zheng YJ, Yamagishi H, Odaka M, Tsujimura M, Maeda M, Endo I (2003) FEBS Lett 553:391–396
32. Murakami T, Nojiri M, Nakayama H, Odaka M, Yohda M, Dohmae N, Takio K, Nagamune T, Endo I (1999) J Inorg Biochem 74:242
33. Murakami T, Nojiri M, Nakayama H, Odaka M, Yohda M, Dohmae N, Takio K, Nagamune T, Endo I (2000) Protein Sci 9:1024–1030
34. Ellis KJ, Lappin AG, Mcauley A (1975) J Chem Soc Dalton Trans 1930–1934

35. Holm RH, Ibers JA (1977) Iron–Sulfur proteins, vol III. Academic Press, New York
36. Chen HW, Lin CW, Chen CC, Yang LB, Chiang MH, Liaw WF (2005) Inorg Chem 44:3226–3232
37. Duff SE, Hitchcock PB, Davies SC, Barclay JE, Evans DJ (2005) Acta Crystallogr Sect E Struct Rep Online 61:M1313–M1315
38. Galardon E, Giorgi M, Artaud I (2004) Chem Commun 286–287
39. Heinrich L, Li Y, Vaissermann J, Chottard G, Chottard JC (1999) Angew Chem Int Ed Engl 38:3526–3528
40. Lee CM, Chen CH, Chen HW, Hsu JL, Lee GH, Liaw WF (2005) Inorg Chem 44:6670–6679
41. Lee CM, Hsieh CH, Dutta A, Lee GH, Liaw WF (2003) J Am Chem Soc 125:11492–11493
42. Noveron JC, Olmstead MM, Mascharak PK (2001) J Am Chem Soc 123:3247–3259
43. Sellmann D, Hein K, Heinemann FW (2004) Inorg Chim Acta 357:3739–3745
44. Deutsch E, Root MJ, Nosco DL (1982) Adv Inorg Bioinorg Mech 1:269
45. Grapperhaus CA, Patra AK, Mashuta MS (2002) Inorg Chem 41:1039–1041
46. Grapperhaus CA, Li M, Patra AK, Poturovic S, Kozlowski PM, Zgierski MZ, Mashuta MS (2003) Inorg Chem 42:4382–4388
47. Grapperhaus CA, Patra AK, Poturovic S (2001) J Inorg Biochem 86:240
48. Gordon AJ (1972) The chemist's companion: a handbook of practical data, techniques and references. Wiley, New York
49. Armarego WLF, Perrin DD (1996) Purification of laboratory chemicals, 4th edn. Butterworth Heinimann, Oxford
50. Shriver DF, Drezdon MA (1986) The manipulation of air-sensitive compounds, 2nd edn. Wiley, New York
51. Bruker Advanced X-ray Solutions (2001) SMART, v5.625. Bruker advanced
52. Bruker Advanced X-ray Solutions (2001) SAINT, v6.22. Bruker advanced
53. Sheldrick GM (1997) SADABS, v2.02, area detector absorption correction. University Gottingen, Gottingen
54. Sheldrick GM (2008) Acta Crystallogr Sect A 64:112–122
55. Frisch MJ, Trucks GW, Schlegel HB, Scuseria GE, Robb MA, Cheeseman JR, Montgomery JA Jr, Vreven T, Kudin KN, Burant JC, Millam JM, Iyengar SS, Tomasi J, Barone V, Mennucci B, Cossi M, Scalmani G, Rega N, Petersson GA, Nakatsuji H, Hada M, Ehara M, Toyota K, Fukuda R, Hasegawa J, Ishida M, Nakajima T, Honda Y, Kitao O, Nakai H, Klene M, Li X, Knox JE, Hratchian HP, Cross JB, Bakken V, Adamo C, Jaramillo J, Gomperts R, Stratmann RE, Yazyev O, Austin AJ, Cammi R, Pomelli C, Ochterski JW, Ayala PY, Morokuma K, Voth GA, Salvador P, Dannenberg JJ, Zakrzewski VG, Dapprich S, Daniels AD, Strain MC, Farkas O, Malick DK, Rabuck AD, Raghavachari K, Foresman JB, Ortiz JV, Cui Q, Baboul AG, Clifford S, Cioslowski J, Stefanov BB, Liu G, Liashenko A, Piskorz P, Komaromi I, Martin RL, Fox DJ, Keith T, Al-Laham MA, Peng CY, Nanayakkara A, Challacombe M, Gill PMW, Johnson B, Chen W, Wong MW, Gonzalez C, Pople JA (2004) Gaussian 03, Revision C.02. Gaussian, Inc., Wallingford
56. Becke AD (1988) Phys Rev A 38:3098–3100
57. Perdew JP (1986) Phys Rev B 33:8822–8824
58. Ghosh P, Bill E, Weyhermuller T, Neese F, Wieghardt K (2003) J Am Chem Soc 125:1293–1308
59. Becke AD (1993) J Chem Phys 98:5648–5652
60. Stephens PJ, Devlin FJ, Chabalowski CF, Frisch MJ (1994) J Phys Chem 98:11623–11627
61. Boone AJ, Chang CH, Greene SN, Herz T, Richards NGJ (2003) Coord Chem Rev 238:291–314
62. Glendening ED, Badenhoop JK, Reed AE, Carpenter JE, Bohmann JA, Morales CM, Weinhold F (2001) NBO 5.0 Theoretical Chemistry Institute, University of Wisconsin, Madison
63. Frisch MJ, Trucks GW, Schlegel HB, Scuseria GE, Robb MA, Cheeseman JR, Zakrzewski VG, Montgomery JA Jr, Stratmann RE, Burant JC, Dapprich S, Millam JM, Daniels AD, Kudin KN, Strain MC, Farkas O, Tomasi J, Barone V, Cossi M, Cammi R, Mennucci B, Pomelli C, Adamo C, Clifford S, Ochterski J, Petersson GA, Ayala PY, Cui Q, Morokuma K, Malick DK, Rabuck AD, Raghavachari K, Foresman JB, Cioslowski J, Ortiz JV, Stefanov BB, Liu G, Liashenko A, Piskorz P, Komaromi I, Gomperts R, Martin RL, Fox DJ, Keith T, Al-Laham MA, Peng CY, Nanayakkara A, Gonzalez C, Challacombe M, Gill PMW, Johnson BG, Chen W, Wong MW, Andres JL, Head-Gordon M, Replogle ES, Pople JA (1998) Gaussian 98. Gaussian, Pittsburgh
64. Humphrey W, Dalke A, Schulten K (1996) J Mol Graph 14:33–38
65. Persistence of Vision Pty. L (2004) Persistence of vision raytracer (version 3.6.). Persistence of Vision Pty. Ltd. Williamstown, Victoria
66. Portmann S, Lüthi HP (2000) Chimia 54:766–770
67. Grapperhaus CA, Darensbourg MY (1998) Acc Chem Res 31:451–459
68. Weinmann DJ, Abrahamson HB (1987) Inorg Chem 26:3034–3040
69. Kubota M, Rothrock RK, Kernan MR, Haven RB (1982) Inorg Chem 21:2491–2493
70. Farmer PJ, Solouki T, Mills DK, Soma T, Russell DH, Reibenspies JH, Darensbourg MY (1992) J Am Chem Soc 114:4601–4605
71. Chandran K, Nithya R, Sankaran K, Gopalan A, Ganesan V (2006) Bull Mater Sci 29:173–179
72. Grapperhaus CA, O'Toole MG, Mashuta MS (2006) Inorg Chem Commun 9:1204–1206
73. Farrugia LJ (1997) J Appl Crystallogr 30:565
74. Sellmann D, Utz J, Heinemann FW (1999) Inorg Chem 38:459–466
75. Sellmann D, Hofmann T, Knoch F (1994) Inorg Chim Acta 224:61–71
76. Sellmann D, Soglowek W, Knoch F, Ritter G, Dengler J (1992) Inorg Chem 31:3711–3717
77. Sellmann D, Soglowek W, Knoch F, Moll M (1989) Angew Chem Int Ed Engl 28:1271–1272
78. Sellmann D, Kunstmann H, Knoch F, Moll M (1988) Inorg Chem 27:4183–4190
79. Henderson RK, Bouwman E, Spek AL, Reedijk J (1997) Inorg Chem 36:4616–4617
80. Kaasjager VE, Bouwman E, Gorter S, Reedijk J, Grapperhaus CA, Reibenspies JH, Smee JJ, Darensbourg MY, Derecskei-Kovacs A, Thomson LM (2002) Inorg Chem 41:1837–1844
81. Grapperhaus CA, Mullins CS, Kozlowski PM, Mashuta MS (2004) Inorg Chem 43:2859–2866
82. Neese F (2006) J Inorg Biochem 100:716–726
83. Chang CH, Boone AJ, Bartlett RJ, Richards NGJ (2004) Inorg Chem 43:458–472
84. Griffith JS (1956) Proc R Soc Lond Ser A 235:23–26
85. Taylor CPS (1977) Biochim Biophys Acta 491:137–149
86. Hagen WR (1992) Adv Inorg Chem Rad 38:165–222
87. Fischer H, Schulz-Ekloff G, Wohrle D (1997) Chem Eng Technol 20:624–632
88. Fischer H, SchulzEkloff G, Wohrle D (1997) Chem Eng Technol 20:462–468
89. Hudlicky M (1990) Oxidations in organic chemistry. American Chemical Society, Washington, DC
90. Oae S (1977) The organic chemistry of sulfur. Plenum, New York
91. Grapperhaus CA, Poturovic S, Mashuta MS (2005) Inorg Chem 44:8185–8187
92. Asano Y, Tani Y, Yamada H (1980) Agric Biol Chem Tokyo 44:2251–2252